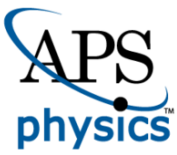

Spiral defect drift in the wave fields of multiple excitation patterns

Sumana Dutta and Oliver Steinbock

Phys. Rev. E **83**, 056213 — Published 20 May 2011

DOI: 10.1103/PhysRevE.83.056213

Spiral Defect Drift in the Wave Fields of Multiple Excitation Patterns

Sumana Dutta and Oliver Steinbock*
Florida State University, Department of Chemistry and Biochemistry, Tallahassee, Florida 32306-4390

Spiral waves in excitable systems decay to drifting defects if forced by high-frequency wave trains. Using the Barkley model, we analyze the drift velocity in planar wave trains as a function of wave frequency. Within two antiparallel, planar wave trains of equal frequency a defect is pushed into the collision region where it stops. Within two circular wave fields, however, it continues its drift in a direction perpendicular to the axis connecting the pacemakers. Depending on the forcing frequency and the initial position, this motion occurs either away from or towards the pacemaker axis. Three circular wave fields can be used to position the defect at a unique point close to the center of the pacemaker triangle. The results are also observed in experiments with the Belousov-Zhabotinsky reaction.

PACS numbers: 05.45.-a, 82.40.Ck, 82.40.Qt
Keywords:

I. INTRODUCTION

Excitation waves are a widespread phenomenon in nonlinear systems and continue to attract scientific interest, especially in the context of reaction-diffusion media. Classic examples include propagating reaction zones on catalytic surfaces [1], spreading messenger signals in aggregating microorganisms [2], and propagating action potentials in the human heart [3]. Recent studies also identified excitation waves as a self-defense mechanism of bee populations [4] and the cause of traveling color bands in the skin of certain mice [5]. All of these wave phenomena show essentially constant front velocities and pulse shapes. In addition, interference phenomena are absent as colliding waves annihilate similar to wildfire fronts.

In spatially two-dimensional systems, excitation waves can organize rotating vortices in which the excitation front is an Archimedean spiral of constant pitch. In these large-scale patterns, the spiral tip is the primary pacemaker. Its frequency as well as its trajectory (*e.g.*, circles and epicycles) are characteristic for a given system, although some systems can show multistable vortex solutions [6, 7]. The spiral tip is also a phase singularity and as such has certain particle-like characteristics [8]. Furthermore, the creation and annihilation of spirals occurs via counter-rotating pairs [9]. Alternatively, spirals may vanish at the system boundaries [10, 11].

Over the past decades numerous approaches have been explored to reposition spiral tips and to induce their annihilation [12–15]. These efforts are motivated partly by the hope to remove rotating action potentials in the human heart where they are believed to cause tachycardia and fibrillation [3, 16, 17]. One approach employs spatially homogeneous variations of system parameters to induce resonant or entrained drift of the spiral tip [18, 19]. This method and related feedback algorithms [20] have been demonstrated primarily for the photosensitive Belousov-Zhabotinsky (BZ) reaction [21]. Other approaches involve parameter gradients (*e.g.*, in temperature) [22] and vectorial perturbations such as applied electric fields [23]. Unfortunately, it is technically challenging or impossible to apply these methodologies to the human heart.

A technically simpler but dynamically more indirect way to induce spiral drift was suggested by the Pushchino group in the mid 1980s [13, 14]. In their studies, spiral waves are perturbed by periodic wave trains of frequencies higher than the frequency of the spiral. A simple way to generate these wave trains is to trigger concentric target patterns from small oscillating or periodically forced regions. With every collision, the demarkation line between the spiral arm and the target waves shifts towards the "slower" spiral tip. When the forcing waves reach the spiral core region, the tip fails to complete its orbit and deteriorates to a mere defect of the growing target pattern. In contrast to the non-translating spiral tip, the defect undergoes translation within the surrounding pattern. In numerical simulations and kinematic models, Krinsky *et al.* showed that this drift can move the defect away or - perhaps more surprisingly - also closer to the fast pacemaker [24]. This drift phenomenon has also been observed in the BZ reaction and in experiments involving colonies of amoeba and slices of cardiac tissue [25–29]. Notice that after cessation of the wave forcing all non-annihilated defects regrow into large spiral wave patterns.

Here we revisit spiral wave defects and their drift dynamics using the Barkley model [30] and experiments employing the autocatalytic BZ reaction. We show that the dependence of the drift direction on the forcing period can be more complex than reported earlier. In addition, we analyze the drift dynamics in the presence of several pacemakers and establish some simple rules for predicting defect drift along the collision regions between those trigger sites.

II. MODEL

For our simulations we numerically integrate the Barkley model

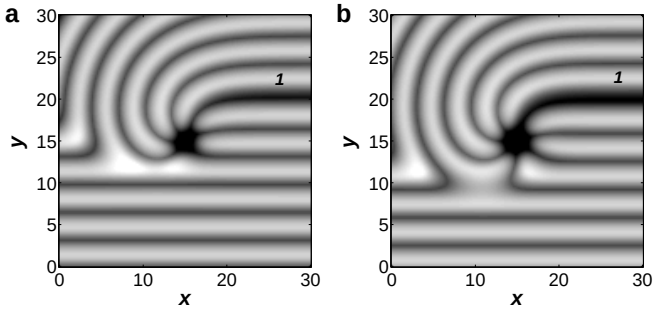

FIG. 1: Simulation of spiral defects in planar wave trains. The frames show the superposition of several snapshots of the V-concentration pattern obtained during approximately one rotation of the defect. The time between subsequent snapshot is 1.5 (dimensionless time units) and the wave from the first snapshot in each frame is labeled as "1". The forcing waves travel in $+y$ direction. The frequency ratio between the forcing waves and the unperturbed spiral wave is 0.80 in (a) and 0.95 in (b). The defect drifts towards the upper left in (a) and towards the (lower) right in (b).

$$\frac{\partial U}{\partial t} = D_U \nabla^2 U + \frac{1}{\epsilon}\left\{U(1-U)\left(U - \frac{V+b}{a}\right)\right\}, \quad (1a)$$

$$\frac{\partial V}{\partial t} = D_V \nabla^2 V + U - V. \quad (1b)$$

In these coupled reaction-diffusion equations U and V are time-dependent variables. We focus strictly on the case of equal diffusion coefficients ($D_U = D_V = 1$). Also the parameters $a = 1.1$, $b = 0.18$, and $\epsilon = 0.02$ are kept constant. The latter values induce excitable point dynamics around a stable steady state. In this system, spiral waves exist and their tips rotate along circular trajectories. These dynamics are referred to as rigid rotation. We identify the spiral tip as the intersections of the u=0.5 and $v = a/2 - b = 0.37$ isoconcentration curves. Our simulations employ Euler integration with a time step of 5×10^{-3}. The Laplacians are computed using the five-point stencil. The system is surrounded by Neumann boundaries and resolved with at least 250×250 but typically 500×500 grid points at a grid spacing of 0.2. Target patterns and planar wave trains are initiated by periodically increasing the value of the activator U within small regions and thin stripes, respectively.

III. COMPUTATIONAL RESULTS

Figure 1 shows two typical examples of spiral defects being forced by planar waves traveling in $+y$ direction. The images are the superposition of six (a) and seven (b) successive V-concentration snapshots obtained during approximately one rotation cycle of the defect. They are computed as the local maxima of these pattern sets and encode the wave positions as bright regions. The most striking features in Fig. 1 are the dynamical quiescent (dark) spiral cores. The defect rotates around these core regions in counter-clockwise direction. The figures also show that the defects tend to create a shock-like line of V-shaped wave segments. Each of these cusps forms in collisions between the round spiral arm and the planar waves.

As described and analyzed in earlier studies, the wave-induced motion of a spiral defect is caused by the repeated collisions between the defect tip with the forcing wave fronts. Consequently, the ratio between the period of free spiral rotation T_{spiral} and the period of the forcing wave train T_{force} is a crucial parameter. In Figs. 1(a,b) this ratio equals 0.8 and 0.95, respectively. Accordingly, the defect tip in (a) undergoes essentially a head-on collision with the planar front, while in (b) it can nearly complete its rotation cycle.

Krinsky *et al.* studied defect motion for the FitzHugh-Nagumo model and suggested several kinematic models. The simplest model describes the drift trajectory as a chain of circular but incomplete spiral tip orbits [13]. The radius of the circular arcs R and the corresponding angular frequency $\omega_{spiral} = 2\pi/T_{spiral}$ are thought to match the parameters of the free spiral. In this chain, each arc segment starts in normal direction to the forcing front during a wave-tip collision and ends in the subsequent collision.

In this model, the drift velocity and direction follow from the time T_{col} between subsequent tip-wave collisions and the length and direction of the secant connecting the start and end point of the corresponding circular arc. A simple geometric analysis yields

$$v_x = \frac{R\ (\cos(\omega_{spiral} T_{col}) - 1)}{T_{col}}, \quad (2a)$$

$$v_y = \frac{R\ \sin(\omega_{spiral} T_{col})}{T_{col}}, \quad (2b)$$

where v_x is the average drift velocity along the planar forcing fronts and v_y the average velocity component in normal direction to the fronts. Negative values of v_x indicate motion away from the spiral arm of the defect, thus increasing the length of the wave front ending in the defect. Furthermore, positive values of v_y imply that the defect moves in the direction of the forcing waves. For instance, the defect in Fig. 1(a), which is pushed towards the upper left corner, has a drift velocity with $v_x > 0$ and $v_y > 0$. Notice that if $v_y \neq 0$, the collision time T_{col} does not equal the forcing period T_{force}. This Doppler effect is described by the implicit equation

$$c_f\ (T_{col} - T_{force}) = R\ \sin(\omega_{spiral} T_{col}). \quad (3)$$

Figure 2(a) shows the dependence of the drift velocity on the employed forcing period in our Barkley model.

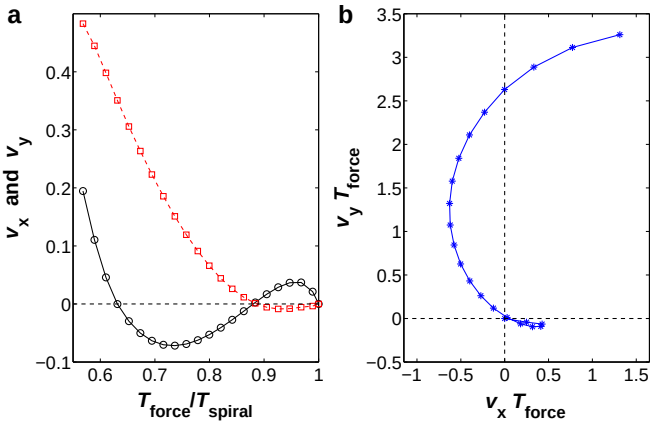

FIG. 2: Color online. Spiral defect motion in planar wave trains computed from numerical simulations. (a) Velocity components v_x (black circles) and v_y (red squares) as a function of the ratio between the periods of the forcing wave train T_{force} and the unperturbed spiral T_{spiral}. The forcing waves travel in $+y$ direction. The defects rotate counterclockwise. (b) Shift in defect position per forcing period obtained from the same data by graphing $v_y T_{force}$ versus $v_x T_{force}$. Notice that drift into three different quadrants is observed.

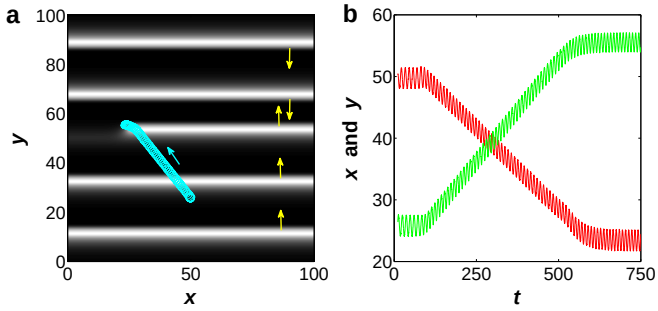

FIG. 3: Color online. Defect drift in the wave field of two planar wave trains. The defect stops within the collision zone of the planar waves. (a) V-concentration pattern of the halted defect with its superposed (cyan) trajectory. The arrows indicate the direction of wave propagation and defect drift. (b) Time evolution of the x (red/ dark gray) and y (green/ light gray) coordinates of the defect tip. Forcing period $T_{force} = 9.5$ and $T_{force}/T_{free} = 0.8$.

The forcing period is rescaled by dividing T_{force} by the rotation period T_{spiral} of freely rotating spiral waves. Notice that period ratios below approximately 0.55 do not yield stable planar wave trains in this system. This limit is due to the absolute refractory zone in the wake of excitation waves. In Fig. 2(b), the same data are replotted in terms of the distances covered by the defect during one forcing cycle. Both graphs show that defect drift occurs into the quadrants I, II, and IV of the Cartesian plane. Defect drift with both negative v_x and negative v_y values (quadrant III) does not exist for the investigated set of model parameters.

The results in Fig. 2 cannot be described by the simple kinematic model in Eqs. (2) because its specific construction of the tip trajectory does not allow for drift into three quadrants. On the contrary, in the model both components of the average drift velocity change their sign only once under variation of the forcing period. Moreover, we conclude that the strongly non-circular shape of the data curve in Fig. 2(b) cannot be described by any model involving simple chains of circular arc segments. It is likely that the primary cause of this discrepancy lies in the positive v_x values found for period ratios T_{force}/T_{spiral} between approximately 0.9 and 1.0. Notice that under this slow forcing the defect tip never fully collides with incoming wave front [see Fig. 1(b)]. The effect of the incoming wave on the tip is rather caused by the V-shaped wave cusp. Due to its high curvature, this cusp accelerates rightwards and thus could cause the unexpected rightward drift of the defect tip. This suggests that the drift behavior computed in this study requires kinematic models that describe the drift trajectory with curves of non-constant radius. However, such modeling efforts are not further pursued here as they are beyond the scope of this work.

The primary focus of this study is the investigation of spiral defect dynamics in systems with *multiple* wave sources. The simplest example involves two planar wave trains of identical frequency that emanate from parallel line sources. Such wave trains collide along a stationary stripe located between the lines of wave initiation. For forcing periods that induce spiral defect drift with $v_y > 0$, any defect will move into the collision region where it experiences forcing from both wave trains. This situation is illustrated in Fig. 3(a). Here downward (upward) propagating planar waves are initiated along the upper (lower) system boundaries. The defect is initially located in the lower wave field and forced to drift towards the upper left corner of the system. This motion brings the defect into the collision region where it stops. The temporal evolution of the corresponding tip coordinates are shown in Fig. 3(b). The data consist of three distinct phases. Initially the planar wave fronts have not yet reached the spiral tip and the tip is stationary. The waves reach the tip at $t \approx 100$ and the expected steady drift commences. Around $t = 600$ the defect reaches the collision zone and its motion ceases.

This phenomenon can be understood qualitatively by considering the spatial symmetry and temporal aspects of the two-wave forcing process in Fig. 3. The stopped defect experiences successive perturbations from collisions with upward and downward moving fronts. The time intervals between these collisions are constant if the defect is located exactly on the collision line of the two wave trains. For such a position, subsequent collisions induce trajectory segments that are the mirror image of each

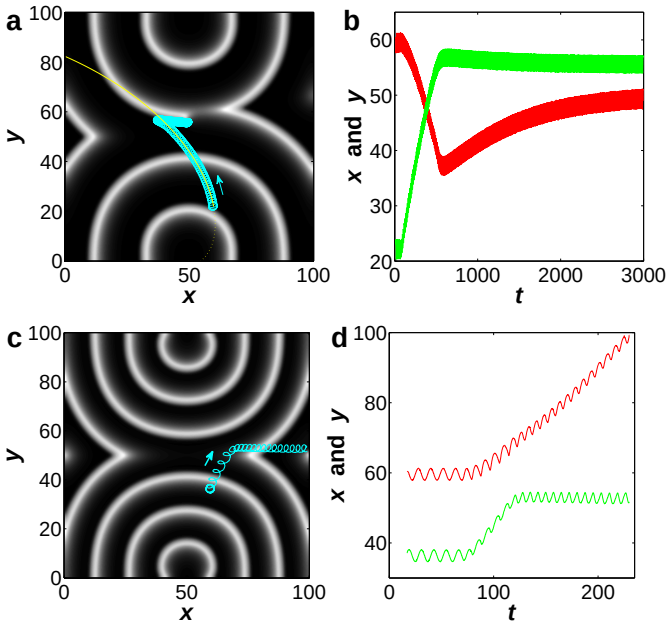

FIG. 4: Color online. Two representative examples of defect drift in the wave field of two circular wave trains. (a,c) V-concentration pattern of the spiral defect with its superposed (cyan) trajectory. The arrows indicate the direction of the defect drift. The smooth (yellow) curve in (a) is a logarithmic spiral. (b,d) Corresponding time evolution of the x (red/ dark gray) and y (green/ light gray) coordinates of the defect tip. The target patterns have frequencies of $T_{\rm force} = 9.5$ in (a,b) and 7.0 in (c,d). Accordingly $T_{\rm force}/T_{\rm spiral}$ is 0.8 in (a,b) and 0.59 in (c,d).

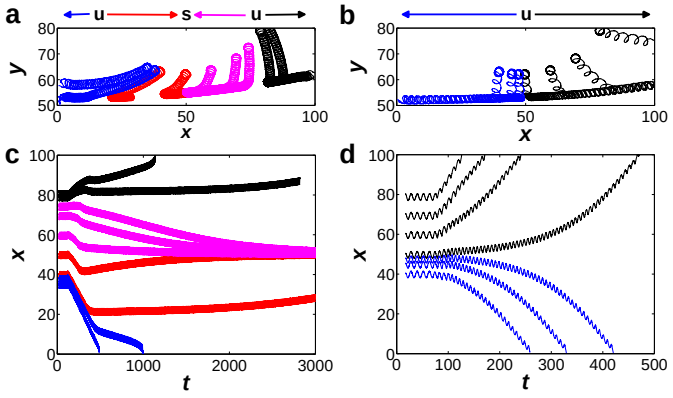

FIG. 5: Color online. Drift trajectories (a,b) and corresponding x coordinates (c,d) of spiral defects with different initial positions. The forcing waves are generated by two target patterns analogous to the situation shown in Fig. 4. The wave periods of the target patterns are $T_{\rm force} = 9.5$ in (a,c) and 7.0 in (b,d). For the lower period, the system shows one stable attractor 's' at x=50 and two repellers 'u' at approximately x=20 and 80. For the higher period, the central point is a repeller. Left and rightward diverging trajectories are plotted in blue and black (darker lines in grayscale), respectively, while attractor-bound curves are shown in red and magenta (lighter lines in grayscale).

other. Consequently no defect motion along the collision line can occur. Moreover, any deviations away from the line (i.e., in upward or downward direction) are counteracted by the normal (single source) drift mechanism.

The timing between subsequent collision events is altered if the collision line separates two *non-planar* wave trains of equal frequency. A simple example of such a scenario is given by two target patterns (Fig. 4). Here circular fronts collide and create V-shaped cusp patterns along the system's horizontal midsection. It was noted elsewhere [25] that defects in (single) circular target patterns drift along trajectories that are well described by logarithmic spirals. This feature is also found in Fig. 4(a) where the initial drift trajectory (cyan line of loops) has been fitted to a logarithmic spiral (smooth yellow curve). More importantly, we find that the defect does not stop once it reaches the collision zone between the two target patterns. It rather performs a sharp turn and continues its motion along the collision line.

We observed that the drift direction in the collision zone depends on the forcing frequency. To illustrate this finding, Fig. 4 shows two examples. In (a,b) the target patterns have a relatively long period with $T_{\rm force}/T_{\rm spiral}$ = 0.8, while in (c,d) forcing is fast with $T_{\rm force}/T_{\rm spiral}$ = 0.59. The corresponding defect motion in the collision zone causes a decelerating drift towards the middle of the system in (a,b) and an accelerating, rightward motion towards the system boundary in (c,d). Notice that slow forcing (a,b) pushes the defect close to the line connecting the two target pacemakers (x = 50 in Fig. 4). This location appears to be a stable attractor for the defect.

As mentioned above, all defect positions along the stationary collision line are stable against perturbations that displace the spiral tip away from this line. The observed drift along the collision line, which was absent in the case of forcing with planar waves, must be due to the different time intervals between wave-defect collisions as well as the different directions of the forcing fronts. For instance, for the case shown in Fig. 4(c,d) the defect first collides with an upward moving wave (lower target pattern), then shortly after with a downward moving wave (upper target), and finally undergoes collision-free motion prior to repeating the cycle. The latter time interval is the longest in this three-step cycle. Also notice that the timing and orientational aspects of this forcing cycle change as the defect is pushed outward. Simulations on very large grids show that the drift velocity approaches the velocity expected for forcing in a single planar wave train. The latter effect is clearly caused by increasing angles between the colliding fronts in the V-shaped cups. For large distances from the pacemaker pair, this angle approaches π and, hence, the case of defect drift in single planar fronts.

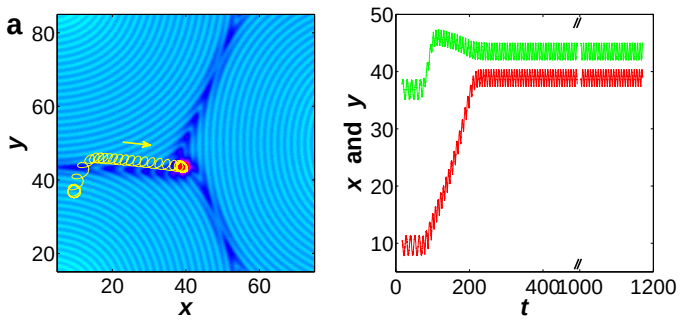

FIG. 6: Color online. Spiral defect drift in the wave field of three circular wave trains. (a) The circular patterns (blue) are the superposition of V-concentration patterns computed during a single forcing period. The collision regions between the three target patterns appear as dark bands. The spiral defect has the lowest V-values and is found around the coordinates $(x, y) = (40, 45)$ (red disk). The defect reached this position along a trajectory shown as a continuous (yellow) line. (b) Corresponding time evolution of the x (red/ dark gray) and y (green/ light gray) coordinates of the defect tip. The three target patterns have identical frequencies and create a forcing period of $T_{\rm force} = 7.0$ ($T_{\rm force}/T_{\rm spiral} = 0.59$).

Further investigations reveal that the direction of the defect drift within the collision zone depends not only the forcing period but also on the exact position of the defect within this region. Figure 5 summarizes the motion of several spiral defects for the fast and slow forcing scenarios that we already analyzed in Fig. 4. We find that for high-frequency pairs of target patterns (Fig. 5(a,c)) the motion is organized by an attractor at x=50 and two repellers around x=20 and 80. If the defect enters the collision zone at a point located between the repellers, it is guided towards the attractor. However, defects outside this interval are pushed away from the attractor and consequently annihilate at the system boundary. For slow forcing (Fig.5(b,d)), the attractor does not exist and only outward motion is observed. The specific frequency-dependent existence of these fixed points suggests that the attractor might be generated in a subcritical pitchfork bifurcation. However, we have not yet systematically explored this interesting feature.

In the following, we consider the case of defect drift in the wave fields of three target patterns. Like in the earlier case, the target patterns have identical frequency. This case is interesting only for conditions that cause outward motion under forcing with two target patterns as inward motion establishes a stable position along one of the axes connecting pairs of pacemakers. The latter situation is obviously identical to the generic case in Fig. 4(a,b). For motion away from this axis, we initially observe behavior analogous to the dynamics in Fig. 4(c,d). However, the combined wave fields of the triple target pattern have a unique point in which waves from all three wave sources collide. This "triple" point is also the terminus of the three collision lines between target pairs and the question arises whether a spiral defect can be parked at this location in a stable fashion.

A typical example of the three-pacemaker scenario is shown in Fig. 6. Here, the wave fields are visualized by superposing V-concentration patterns computed during one forcing period. The individual pacemakers are located in the upper left corner, the lower left corner, and at the midpoint of the right system boundary. The defect trajectory is superposed as a continuous line. It shows that the defect first moves out of the wave field created by the lower left pacemaker, then travels rightwards under the influence of the two target patterns in the left half of the system, and finally stops due to interactions with all three wave fields. In Fig. 6(a), the collision lines are darker (blue) stripes and the final location of the defect can be discerned from a disk shaped (red) region that corresponds to the spiral core. The temporal evolution of the Cartesian coordinates of the defect in Fig. 6(b) indicate that this position is stationary.

IV. EXPERIMENTAL METHODS

In the second half of this Article, we show that the defect dynamics found in numerical simulations can also be observed in experimental systems. Our specific experiments use the chemical Belousov-Zhabotinsky (BZ) reaction, which is a frequently studied excitable reaction-diffusion system [31, 32]. The BZ reaction involves the bromination of an organic compound (here malonic acid) by bromate in acidic solution. Its key step is the autocatalytic, and hence nonlinear, production of bromous acid. We prepare the BZ reaction with the catalyst ferroin/ferriin. The latter redox couple undergoes striking color differences during each excitation cycle, which allows for the optical detection of the excitation waves.

Our experiments employ thin layers of the reaction media that are either contained in a gel or liquid phase. In either case the layer height is 2.0 mm. We found no evidence of undesired hydrodynamic flows. The experiments with single forcing patterns were carried out in agarose gel (0.8 % weight/volume). Disregarding the bromination of malonic acid, the initial reactant concentrations are $[H_2SO_4] = 0.16$ mol/L, $[NaBrO_3] = 0.04$ mol/L, [malonic acid] = 0.04 mol/L, and $[Fe(phen)_3SO_4] = 0.5$ mmol/L (concentration set I). In the case of multiple forcing patterns and to decrease the time of the experiments, we used an alternative composition, which we refer to as concentration set II. The initial reactant concentrations in liquid phase are $[H_2SO_4] = 0.41$ mol/L, $[NaBrO_3] = 0.3$ mol/L, [malonic acid] = 0.2 mol/L, and $[Fe(phen)_3SO_4] = 3.75$ mmol/L. The solutions are prepared in nanopure water (18 MΩcm) and all experiments are carried out at room temperature.

The chemical waves in this system are monitored based on their spatio-temporal transmittance patterns. For

this purpose, the sample is illuminated with white light (Fiber-Lite PL-800) and the transmitted light is detected by a charge-coupled device camera mounted over the reaction layer. This method utilizes the color difference between the chemically reduced rest state (red) and the oxidized, excited state (blue). The position of spiral defects are measured from sequences of video frames by locating the point of highest curvature at the open wave ends.

For the creation of high frequency wave patterns, we modify the system dynamics in small regions of the active BZ layer. This modification is accomplished by injection of a small drop (~ 1 μL) of sulfuric acid (1 mol/L) or BZ solution with a higher bromate concentration (0.3 mol/L). The latter (former) perturbation is used for gel (liquid) systems. Typically the affected regions develop spiral waves. These spirals have a higher frequency than the spirals and target patterns in the unaffected surroundings and hence quickly create a large wave pattern. Within this pattern, we create defect pairs by inserting a microscope cover slip parallel to the wave fronts. This thin piece of glass is a physical boundary and, hence, impenetrable to the traveling waves. After blocking at least one wave front, the obstacle is removed, which nucleates the desired defect pair. Notice that the distance between the studied defects and the injection site is at least 1 cm. Since our experiments last less than one hour, the system around the defect is not affected by diffusion of injected solution but only by the altered frequency of chemical waves generated in this region.

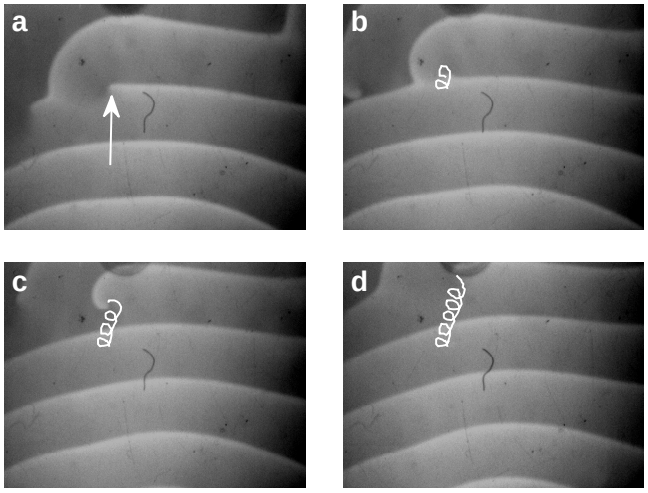

FIG. 7: Defect drift in a thin layer of the Belousov-Zhabotinsky system. The time between subsequent snapshots is 940 s. The forcing waves travel in upward direction. The frequency ratio between the forcing waves and the unperturbed spiral wave is 0.57. The defect drifts towards the upper right corner tracing the white trajectories superposed on frames (b-c). The white arrow in (a) marks the initial position of the defect. The initial reactant concentrations are listed in the text as set I. The field of view is 2.44×1.83 cm^2.

V. EXPERIMENTAL RESULTS

Figure 7 shows a sequence of snapshots recorded for a typical example of defect drift in the BZ system. The reaction is carried out in a thin gel layer and for the concentrations specified in set I. The bright bands correspond to regions in which the catalyst is predominantly oxidized. The actual excitation pulse is located at the leading edge of these bands (not measured) where the concentration of the activator bromous acid is expected to be high. In the wake of the bright bands, the system is refractory due to a high concentration of the inhibitor bromide. The arrow in Fig. 7(a) indicates the initial position of the defect. The drift trajectory is superposed as white curves that extend from the defect's initial location to its position in the given image frame. The forcing waves have a period of $T_{\rm force} = 186$ s while free spirals in this system have a period of $T_{\rm free} = 325$ s ($T_{\rm force}/T_{\rm free}$=0.57). The upward traveling waves have a low front curvature and force the defect in a nearly constant direction. Notice that the defect in Fig. 7 rotates in counter-clockwise direction.

As expected our experiments show that the drift velocity and the drift direction depend strongly on the period of the forcing wave train. The corresponding results are summarized in Fig. 8. The data are obtained from defects drifting in wave trains that have low front curvature and constant periods. Notice that the rotation period of the free unperturbed spiral equals $T_{\rm spiral} = 325$ s. We successfully varied the forcing period down to approximately 170 s. Attempts to trigger waves with even shorter periods failed and usually resulted in a "thinning" of the wave train by self-elimination of every second wave pulse. Notice that the existence of such a high-frequency limit is typical for excitation waves and related to their absolute refractory zone [33]. Furthermore, Fig. 8 shows that the sign of the velocity component v_y changes once over the range of accessible forcing periods. As in Fig. 2(a), negative values of v_y (red squares) indicate a defect drift against the forcing wave motion. The v_x component (black circles in Fig. 8), however, changes sign twice in the range of possible forcing periods. The latter finding is in good qualitative agreement with the numerical results in Fig. 2.

In order to understand defect dynamics in the wave field of multiple target patterns, we performed experiments with more than one region of high-frequency wave generation. These regions are created by careful injection of sulfuric acid into several, well separated sites of the active system. Moreover, all of the following experiments employ a BZ medium with initial concentrations specified by the parameter set II. The rotation period of unperturbed spiral waves in this system is 18.0 s. For this excitable medium, Fig. 9 shows an example of defect drift under the influence of two forcing patterns. The patterns have an almost identical frequency of 10.0 s with right-

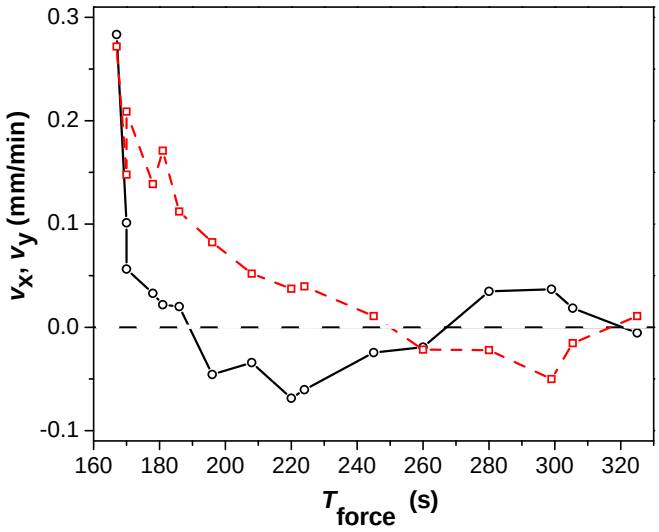

FIG. 8: Color online. Drift velocity of spiral defects in single, near-planar wave trains as a function of the forcing period. The values of v_x (black open circles) describe the velocity component along the forcing wave fronts, while v_y (red squares) is the velocity component perpendicular to the forcing waves. The experiments were carried out for reactant concentrations described by set I.

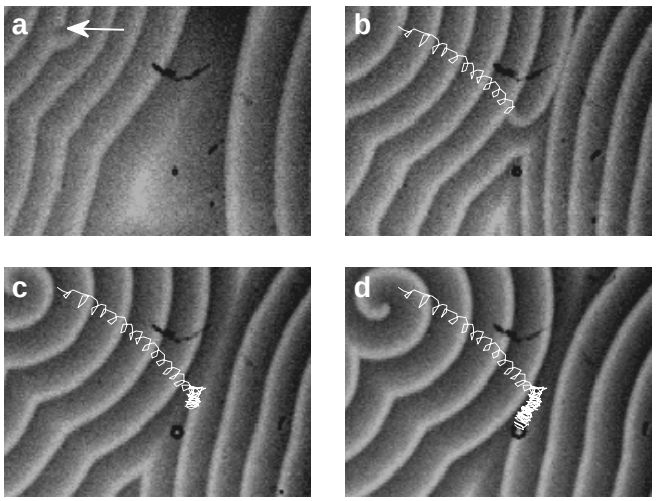

FIG. 9: Defect drift in the wave field of two pacemakers. The forcing waves have a period of $T_{\rm force} = 10$ s. The arrow in (a) indicates the initial position of the defect. The superposed white curves (b-d) show the drift trajectory. Images are recorded at an interval of 122 s. Rotation period of the unperturbed spiral: $T_{\rm spiral} = 18$ s. Field of view : 6.2×4.6 mm^2. The experiments were carried out for reactant concentrations described by set II.

ward moving (three to five o'clock direction) waves in the left portion of the images and leftward traveling waves in the right third. In Fig. 9(a) a single defect is located in the upper left portion of the image (white arrow in Fig. 9(a)). Its sense of rotation is clockwise. During the course of about two minutes, the defect is pushed into the collision zone of the two high-frequency wave patterns. In Figs. 9(b-d) the drift trajectory is superposed as white curves. Notice that each curve extends only up to the location of defect in the corresponding image. Once the defect has reached the collision zone, its drift velocity and direction change. As shown in Figs. 9(c,d), the defect continues its motion within the collision zone in a downward direction. This direction is marked by increasing angles between the colliding, high-frequency fronts. The drift scenario in Fig. 9 is therefore comparable to the simulated outward motion in Fig. 4(c,d).

Our results have shown that longer forcing periods can cause a sign change in the v_x component of the drift velocity that results in a reversed drift direction of defects perturbed by two curved wave trains (see Fig. 4(a,b)). This situation is illustrated in Fig. 10 where the forcing period is approximately 12 s and the sign of the v_x component reversed with respect to Fig. 9. Notice that the defect is rotating counter clockwise. The image sequence in Fig. 10 shows that the defect (marked by a white arrow in (a)) is pushed into the collision zone where it abruptly changes direction. In contrast to Fig. 9, the defect then moves into a region of decreasing angles between the colliding fronts.

We also attempted to perform experiments in which the two forcing wave trains are planar. Based on our simulations (see Fig. 3), this situation is expected to stop defect drift in the collision zone. While it is very difficult to prepare this scenario in experiments, we did obtain a few examples that indeed show this behavior but typically in complicated wave patterns. One of these experiments is illustrated in the supplementary information file [34]. The latter also contains data on defect dynamics in the wave field of two wave trains that differ in period. Under such conditions, the defect is initially pushed into the collision zone. Due to the frequency differences this zone is not stationary but shifts towards the lower frequency side and the defect follows this motion.

Lastly we report defect drift in systems with three high-frequency wave patterns of approximately equal period. Figure 11(a) shows the trajectory of a defect under such a condition, which consists of (i) a long, slightly arched initial part, (ii) a sharp right-turn, and (iii) an essentially stationary orbit (preceded by a small downward correction). These stages correspond to (i) drift in a single (slightly curved) wave train, (ii) motion along the boundary of two wave patterns, and (iii) stable rotation at the "triple point" of the three wave patterns. The latter location is the common end point of the collision lines between the three pairs of wave trains. The rotation pattern of the defect at this point is unusual in the sense that each rotation cycle involves three wave-tip collisions. This feature is illustrated in Fig. 11(b) which is constructed by image addition of three snap-

shots recorded at time intervals of approximately one third of the forcing period. The defect can be discerned as a triskelion (three-armed "swastika") in the mid region of the image. Notice that the two freely rotating spiral waves in the lower left corner have a strikingly different structure.

In summary, we have studied the motion of spiral defects in single and multiple wave trains. These defects form if spirals are exposed to wave patterns with frequencies higher than the rotation frequency of the vortex. The qualitative characteristics of the defect motion are widely independent of the specific features of the excitable system. They can be summarized as follows: (i) in planar wave trains the defect moves with a constant velocity along a straight trajectory. The speed and direction varies with the frequency of the wave train. Defects can be attracted into the nucleation region of the perturbing wave train ($v_y < 0$) but the specific range of drift directions depends on the system. (ii) Defect motion in single, circular wave trains traces logarithmic spirals. Their chirality depends on the rotation sense of the defect and also on the sign of the lateral drift velocity v_x. (iii) Defects in systems with two forcing patterns move into the collision zone as long as $v_y > 0$. If the forcing waves are planar, the defect stops close to the collision line. For curved waves, however, it changes direction and moves along the collision line. Depending on the forcing period and its position, the drift occurs in the direction of either increasing or decreasing angles between the colliding fronts. In the latter case, the defect settles at a point close to the axis that connects the two high-frequency pacemakers. (iv) In systems with three (or more) wave patterns, the global wave pattern is partitioned into a corresponding number of basins. In each basin, all points experience excitation from waves that nucleated from the same pacemaker. The boundaries of the basins define a network of collision lines. Defects in such systems can move to the triple points of this network, which then are stable attractors.

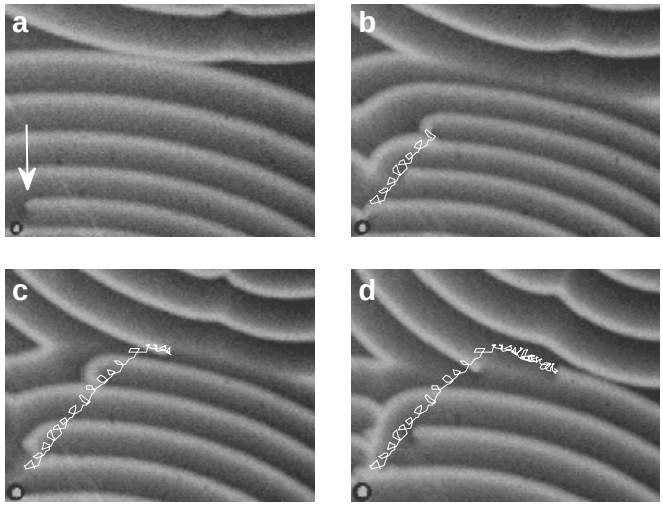

FIG. 10: Defect drift in the wave field of two pacemakers. The forcing waves have a period of $T_{\rm force} = 12$ s. The arrow in (a) indicates the initial position of the defect. The superposed white curves (b-d) show the drift trajectory. Images are recorded at an interval of 200 s. Rotation period of the unperturbed spiral: $T_{\rm spiral} = 18$ s. Field of view : 6.7×5.0 mm^2. The experiments were carried out for reactant concentrations described by set II.

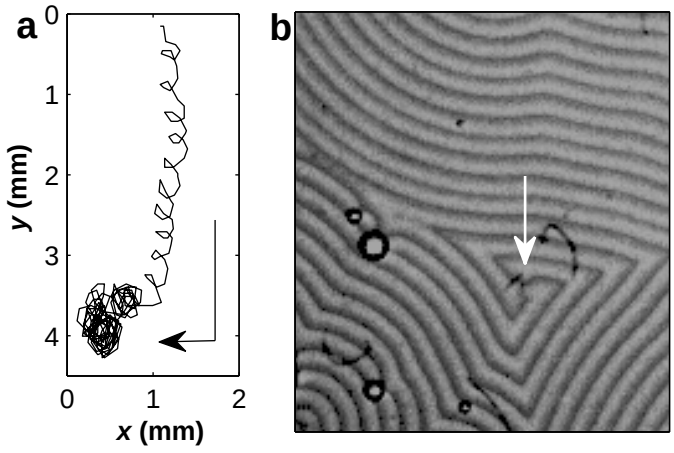

FIG. 11: Defect dynamics under the influence of three forcing wave patterns. (a) Trajectory of the spiral defect. (b) Superposition of three snapshots obtained from the same experiment after the defect reached its final position. The time between each snapshot corresponds to one third of the forcing period. The arrow in (b) indicates the final position of the defect. Field of view : 7.0×7.9 mm^2. The experiments were carried out for reactant concentrations described by set II.

A potentially interesting complication arises if the system has several defects. In this situation, one of the defects will reach the original collision line first and subsequently alter the shape of the later. This deformation of the collision line can be discerned in Fig. 4(a), where the two initially symmetric collision-induced wave cusps (not shown in the figure), are now offset in vertical direction by about 10 space units. If there is a second defect present in the system, it will drift along this new collision line. Additional work is needed to describe and analyze the resulting dynamics and asymptotic defect locations.

VI. CONCLUSIONS

Despite this current limitation, wave forcing offers several tools for the positioning of spiral waves in specific regions of an excitable system. These procedures are unique in the sense that they can be implemented from a small number of perturbation sites located at the boundaries of the system. For instance, if the goal is the annihilation of a vortex at the system boundary, it is suf-

ficient to create a target pattern from a single point on the system boundary with a frequency that gives rise to negative $y-$component of the drift velocity. Moreover, two trigger points are sufficient to attract the spiral to any desired line. Within the appropriate range of forcing frequencies, two and three trigger points allow the placement of the spiral at a specific point. We believe that such remote-positioning protocols are also the most efficient strategy for changing the location of vortices in three-dimensional systems. Notice that in 3D most global perturbations (e.g., heat and light) are affected by undesired gradients and/or temporal delays. It will hence be interesting to extend our studies to systems such as the three-dimensional BZ reaction or three-dimensional samples of cardiac tissue [3, 35]. However, one can expect that the response of vortices (scroll waves) in these systems is more complicated as spiral rotation occurs around one-dimensional filaments rather than the pseudo-one dimensional core region of the vortex.

ACKNOWLEDGEMENTS

This material is based upon work supported by the National Science Foundation under Grant No. 0910657.

[1] D. Krefting, P. Kaira, H. H. Rotermund, Phys. Rev. Lett. **102**, 178301 (2009).
[2] S. C. Müller, T. Mair, O. Steinbock, Biophys. Chem. **72**, 37 (1998).
[3] E. M. Cherry, F. H. Fenton, New J. Phys. **10**, 125016 (2008).
[4] G. Kastberger, E. Schmelzer, I. Kranner, PLoS ONE **3**, e3141 (2008).
[5] N. Suzuki, M. Hirata, S. Kondo, Proc. Natl. Acad. Sci. USA **100**, 968 (2003).
[6] A. T. Winfree, Physica D **49**, 125 (1991).
[7] M. Br, N. Gottschalk, M. Eiswirth, G. Ertl, J. Chem. Phys. **100**, 1202 (1994).
[8] I. V. Biktasheva, D. Barkley, V. N. Biktashev, A. J. Foulkes, Phys. Rev. E **81**, 066202 (2010).
[9] J. Schütze, O. Steinbock, S. C. Müller, Nature (London) **356**, 45 (1992).
[10] J. M. Davidenko, A. M. Pertsov, R. Salomonsz, W. Baxter, J. Jalife, Nature **355**, 349 (1992).
[11] I. Schebesch, H. Engel, Phys. Rev. E **60**, 6429 (1999).
[12] R. M. Zaritski, A. M. Pertsov, Phys. Rev. E **66**, 066120 (2002).
[13] V. I. Krinsky, K. I. Agladze, Physica D **8**, 50 (1983).
[14] Y. A. Yermakova, V. I. Krinskii, A. V. Panfilov, A. M. Pertsov, Biophysics **31**, 348 (1986).
[15] G. Yuan, G. Wang, S. Chen, Europhys. Lett. **72**, 908 (2005).
[16] F. X. Witkowski, L. J. Leon, P. A. Penkoske, W. R. Giles, M. L. Spano, W. L. Ditto, A. T. Winfree, Nature (London) **392**, 78 (1998).
[17] J. Jalife, R. A. Gray, G. E. Morley, J. M. Davidenko, Chaos **8**, 79 (1998).
[18] K. I. Agladze, V. A. Davydov, and A. S. Mikhailov, JETP Lett. **45**, 767 (1987).
[19] O. Steinbock, V. S. Zykov, and S. C. Müller, Nature (London) **366**, 322 (1993).
[20] V.N. Biktashev and A.V. Holden, J. Theor. Biol. **169** 101 1994.
[21] O.-U. Kheowan, V. S. Zykov, O. Rangsiman, S. C. Müller, Phys. Rev. Lett. **86**, 2170 (2001).
[22] M. Vinson, S. Mironov, S. Mulvey, A. Pertsov, Nature (London) **386**, 477 (1997).
[23] O. Steinbock, J. Schütze, S. C. Müller, Phys. Rev. Lett. **68**, 248 (1992).
[24] G. Gottwald, A. Pumir, V. Krinsky, Chaos **11**, 487 (2001).
[25] N. Manz, O. Steinbock, J. Phys. Chem. A **108**, 5295 (2004).
[26] K. J. Lee, E. C. Cox, R. E. Goldstein, Phys. Rev. Lett. **76**, 1174 (1996).
[27] K. J. Lee, Phys. Rev. Lett. **79**, 2907 (1997).
[28] S. Woo, J. H. Hong, T. Y. Kim, B. W. Bae, K. J. Lee, New J. Phys. **10**, 015005 (2008).
[29] J. M. Davidenko, P. F. Kent, D. R. Chialvo, D. C. Michaels, J. Jalife, Proc. Natl. Acad. Sci. USA **87**, 8785 (1990).
[30] R. Mantel, D. Barkley, Physica D **149**, 107 (2001).
[31] A. N. Zaikin and A. M. Zhabotinsky, Nature (London) **225**, 535 (1970)
[32] I. R. Epstein, J. A. Pojman, O. Steinbock, Chaos **16**, 037101 (2006).
[33] J. Rinzel, and J. B. Keller, Biophys. J. **13**, 1313 (1973).
[34] See EPAPS Document No. [] for additional analyses of experimental data.
[35] T. Bánsági, Jr., O. Steinbock, Phys. Rev. Lett. **97**, 198301 (2006).